


Structure, stability, and electro-optic features of nematic drops in 1'',7''-bis(4-cyanobiphenyl-4'-yl)heptane–surfactant binary systems

K. S. Krishnamurthy ^{*}, D. S. Shankar Rao, Shreya Sharma, and Channabasaveshwar V. Yelamagad
Centre for Nano and Soft Matter Sciences, Survey No. 7, Shivanapura, Bangalore 562162, India



(Received 17 January 2022; accepted 11 February 2022; published 28 February 2022)

Binary mixtures of the mesogen [1'',7''-bis(4-cyanobiphenyl-4'-yl)heptane] and a long chain amphiphile (e.g., 2-octadecoxypropanol) are examined for the structure, stability, and electro-optical behavior of nematic drops dispersed in the isotropic phase, in planar cells. Subjected to tangential boundary conditions, the drops adopt, besides the escaped concentric and untwisted bipolar geometries, the less common bound vortex geometry with a pair of half-strength disclination lines. The concentric drop, as it grows, switches its axis from an in-layer to the layer-normal direction corresponding to the stablest of all geometries. Bipolar drops in equilibrium have their axes parallel to the easy axis of the cell. Obliquely oriented bipolar drops rotate to attain the equilibrium disposition by the shorter of the clockwise and anticlockwise routes, the extent of rotation decreasing exponentially with time. The bipolar structure is marginally less stable than the concentric, and transforms to the latter geometry occasionally. In bound vortex drops, the separation between the lines varies as the drop diameter, the bipolar and concentric geometries appearing as the limiting cases. The complex course of Fréedericksz transition in all the different types of drops terminates in the division of the original large drop into many smaller drops, each with a surface charge 2, in conformity with the Poincaré-Hopf theorem. In low frequency electric fields, concentric drops exhibit flexoelectro-optic rotation in evidence of their escaped character.

DOI: [10.1103/PhysRevE.105.024709](https://doi.org/10.1103/PhysRevE.105.024709)

I. INTRODUCTION

The orientational structure and electro-optical behavior of nematic droplets dispersed in a solid or fluid matrix have been an area of great theoretical and technological interest, particularly since the advent of optical devices based on polymer dispersed liquid crystals [1–5]. The director field in a nematic drop is determined by the total elastic free energy of distortion F_e relative to the anchoring energy F_s that represents the angle-dependent part of the total interfacial energy; for a spherical drop of radius R , F_e is proportional to KR , K being the elastic constant in one-constant approximation [$K = K_{11}$ (splay) = K_{22} (twist) = K_{33} (bend)], while F_s varies as WR^2 , W being the anchoring coefficient [6,7]. For $F_e \ll F_s$ or $R \gg K/W$ (the extrapolation length), the preferred surface anchoring prevails and the \mathbf{n} field in the drop gets accordingly modified. For typical values of K (~ 1 pN) and W ($\sim 1 \mu\text{J}/\text{m}^2$ for weak anchoring), the critical radius $R_c = K/W$ below which the elastic term gains dominance is $\sim 1 \mu\text{m}$. A drop with $R \gg R_c$ and the director \mathbf{n} along its surface normal \mathbf{k} (homeotropic anchoring) often adopts the radial hedgehog configuration, characterized by a central point defect of charge +1 and a purely splay type distortion around it. There exist other topologically equivalent configurations for homeotropic boundary alignment, described as twisted radial, escaped radial, and axial [8]. Regardless of the structure, as long as \mathbf{n} is along \mathbf{k} , a total topological charge $Q = +1$ (i.e., half the Euler characteristic χ for a sphere) resides in the spherical volume,

in accordance with the Gauss-Bonnet theorem [7,9,10]. On the other hand, when the surface anchoring is tangential, as is found for the N drops examined in the present study, the defect configurations obey the Poincaré-Hopf theorem that stipulates the total topological surface charge s to be equal to χ , i.e., +2 for a spherical drop [6,9–11]. In Fig. 1, we show schematically the possible director configurations for the tangential case, all with $s = 2$. The bipolar structure B is by far the commonest in conventional rodlike systems. It has the splay distortion at the poles and bend along the field lines between them; the radial fields around the two surface point defects (boojums) account for $s = 2$. The twisted bipolar structure TB is known to occur when the elastic moduli are such that $K_{11} \geq K_{22} + 0.431K_{33}$ [9,12]. Concentric nematic droplets C with axial line disclinations are not observed in most rodlike molecular systems in which $K_{33} > K_{11} > K_{22}$, since this geometry is known to require low values (< 1.0) of the ratio K_{33}/K_{11} [4,13]. Clearly, N_{TB} compounds known for their relatively very low K_{33} values in the N phase, close to the N - N_{TB} transition point, are the best candidates when searching for concentric drops. In fact, recent studies with mixtures of the nematogen TL203 (from Merck) and CB7CB have demonstrated [14] the transition from bipolar to concentric around $K_{33} = K_{11}$. Apart from this result relevant to our study, we need to mention the recent reports by Hu *et al.* [15] and Wu *et al.* [16] of defect patterns in N drops. The analytical-numerical study [15] of spherical droplets (three-dimensional, 3D) and disks (two-dimensional, 2D) under different boundary conditions, based on the Landau–de Gennes model, has shown that the +1 line disclination is stable in these systems only for high values of rescaled (dimensionless) temperature and elastic constant;

^{*}murthyksk@cens.res.in

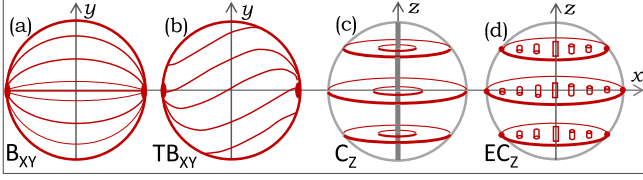


FIG. 1. (a)–(d) Schematic of the director field corresponding to bipolar (a), twisted bipolar (b), concentric (c), and escaped concentric (d) configurations of a nematic drop; the director streamlines are the continuous brown lines. In (d), the cylinders shown along x indicate the director twist about the radius leading to a nonsingular core and singular point terminations of the $+1$ linear disclination.

for low values, this line quantizes into a pair of $+\frac{1}{2}$ lines and, in disks, the half-line pair is the stablest of all possible defects. Our experimental findings here seem to support this prediction of stable existence of the $\frac{1}{2}$ line pair. In the other simulation work based on the Landau–de Gennes theory [16], structural modifications within the droplets due to their varying size are predicted. We find a similar modification trend in our experiments.

We have earlier, in the course of our investigations on some unconventional topological colloids composed of N_{TB} droplets dispersed in their own N phase [17,18], reported on the occurrence of (i) elastic dipoles consisting of droplet monopoles and their counterdefects generated in the nematic, (ii) quadrupoles resulting from the transformation of hyperbolic hedgehogs into Saturn rings, (iii) dipole chains and, in twisted nematic environment, knotted quadrupole assemblies, (iv) defect mediated growth of N_{TB} drops into complex forms, and (v) flexoelectric as well as backflow-induced dynamical features associated with dipoles. In a continuation of our study of these colloidal systems, here we focus mainly on the morphological and dynamical aspects of N drops suspended in the extended I phase of planar samples. Among the important results discussed are the (i) formation of escaped concentric drops with their axes in the layer plane and switching of the axes to layer-normal direction in larger drops, (ii) bipolar to escaped concentric transition, (iii) formation of bound-vortex drops with a pair of $+\frac{1}{2}$ disclinations separated by a distance that varies linearly with the drop diameter, (iv) rotation of twisted bipolar drops toward untwisted equilibrium configuration with the rotation angle varying exponentially with time, (v) complex course of Fréedericksz distortion terminating in multiple divisions of the drop, and (vi) flexoelectro-optic effect in escaped concentric drops. Our presentation of these results in Sec. III is supplemented by nine video clips, some optical textures, and related notes; these are accessible in the Supplemental Material (SM) [19].

II. EXPERIMENTS

The twist-bend nematogen 1'',7''-bis(4-cyanobiphenyl-4'-yl)heptane (CB7CB) used was synthesized by two of the authors (S.S. and C.V.Y.). The phase transitional sequence in CB7CB, from polarization microscopy, was N_{TB} (103.3 °C), N (116.5 °C, T_{NI}), I . In order to obtain a sufficiently wide (a few °C) N - I coexistence region, binary mixtures of CB7CB

with varying quantities of a surfactant—1-tetradecanoic acid (TA), 2-octadecyloxypropynol (OP), 2-docosanoxypropanol (DP), or 2-hexadecyloxybutanol (HB)—were used. The mixtures are specified as $C\ TA_i$, $C\ OP_i$, $C\ DP_i$, and $C\ HB_i$, where C denotes CB7CB, and i the wt % concentration of the amphiphile. The surfactant concentration was 3–5 wt % in most experiments; with higher concentrations and decreasing temperature, there was an increasing tendency for the surfactant rich phase to separate out into tiny droplets. A typical phase diagram is shown in Fig. S1 of the SM in Ref. [17]. In COP5, with which this study is mostly concerned, the I - N transition occurred at 99 °C and the N - N_{TB} (twist-bend nematic) transition, at 89 °C. Between these temperatures, N drops coexisted with the surrounding I matrix. On a prolonged use of the mixtures, particularly in high electric fields, we noticed a slight degradation of the sample leading to a decrease in the transition temperatures by 1 °C–2 °C, but this did not affect the morphological and electro-optic properties of the drops investigated. The permittivity anisotropy ($\epsilon_a = \epsilon_{||} - \epsilon_{\perp}$) for the pure CB7CB sample used in the mixtures was positive, being approximately 1.6 for reduced temperature $T_r = T_{NI} - T = 2$ °C. In the mixtures, it varied very little, being, for example, 1.4 in CHB3 at the same T_r . Optical textures were examined using a Carl Zeiss Axio Imager.M1m polarizing microscope equipped with an AxioCam MRc5 digital camera. The sample cells (from M/s AWAT, Poland), were sandwich type, made of polyimide-coated, unidirectionally buffed ITO electrodes, providing uniform planar orientation of the nematic director \mathbf{n}_o ; the cell gap d was 20 μm unless otherwise stated. An Instec HCS402 hot stage coupled to a STC200 temperature controller maintained the sample at the desired temperature T to an accuracy of ± 0.1 °C. A Stanford Research Systems function generator (DS345) coupled to a FLC Electronics voltage amplifier (model A800) was employed for electro-optic studies. The field frequency f and rms voltage U were measured with a Keithley-2002 multimeter. We use a Cartesian reference system with the axes x and z along the rubbing and observation (or electric field) directions, respectively; $P(\alpha)$ – $A(\beta)$ indicates the setting of the polarizer P and analyzer A with their axes at angles α and β (degrees) relative to x .

For determining the director distribution within structurally different nematic droplets, in addition to the usual polarization microscopic technique, we used the self-decoration pattern of stripes due to surface quasiperiodic alignment modulation (SQAM), which is unique to nematics formed of bent shaped molecules, whether of rigid or flexible core. We have earlier discussed [20] this microscale pattern as arising from nanoscale short-range order clusters dotting the surface and inducing a quasiperiodic splay-bend distortion therein, with the wave vector $q = W\sqrt{K_{11}K_{33}}$, where W is the anchoring energy term. The quasiperiodic distortion is revealed through its lens action on the incident light. The corresponding optical pattern of fluctuating stripes appears in either the real or virtual focal plane. The stripes actually outline the director normal, \mathbf{n}_{\perp} ; they appear with maximum contrast in light linearly polarized, with the electric vector E along the wave vector q , and disappear for E normal to q . Thus, with circularly polarized light, the entire \mathbf{n}_{\perp} map around a disclination becomes visible.

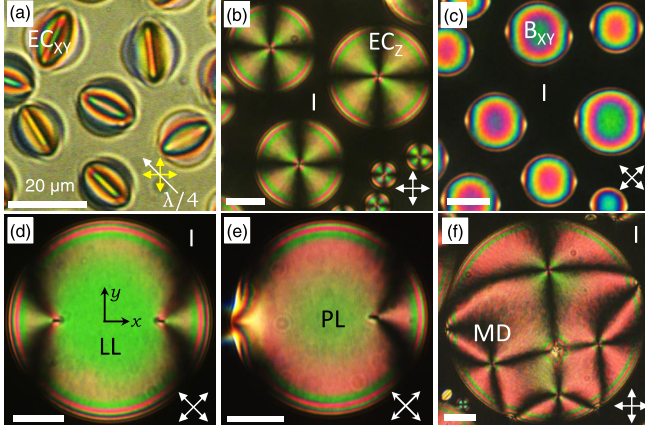


FIG. 2. Typical textures of nematic drops with varying orientational structure observed in the N - I coexistence region of CB7CB-surfactant binary systems. (a) Escaped concentric or toroidal drops EC_{XY} with their axes in the xy plane; COP3. (b) Escaped concentric drops EC_Z with their axes along z ; COP5. (c) Bipolar drops B_{XY} with their axes in the xy plane; CTA5. (d) Bound vortex drop with a pair of $+\frac{1}{2}$ disclination lines, LL; COP5. (e) Hybrid drop with the pole-half-line combination; PL; COP5. (f) Multiple defects drop MD; COP5. $d = 20 \mu\text{m}$. $T = 92^\circ\text{C}$ (a), 91°C (b), (d), (e), 100°C (c), 90°C (f). Double arrows indicate the transmission axes of polarizers.

III. RESULTS AND DISCUSSION

A. Nematic drops: Types observed in planar cells

Seen at a glance in Fig. 2 are the textures of different types of nematic droplets observed in CB7CB-surfactant mixtures in general. They are all structurally consistent with tangential boundary conditions, as also with the Poincaré-Hopf theorem requiring a total surface charge of 2. Notably, besides both the escaped concentric [EC_{XY} and EC_Z , Figs. 2(a) and 2(b)] and bipolar [B_{XY} , Fig. 2(c)] drops, we find drops with two uncommon configurations: one of them, LL, contains a pair of $+\frac{1}{2}$ lines [Fig. 2(d)] and the other, PL, a line-boojum pair [Fig. 2(e)]. Metastable multiple defect configurations (MDs), such as in Fig. 2(f), transform in time to the minimum defect(s) state, while adhering to the topological constraints all through this process.

When a given mixture like COP5 in a planar untwisted cell is gradually cooled from the isotropic phase, at the onset of the N - I transition, typically we observe N droplets nucleating randomly, as in Fig. 3(a). They display extinction brushes along the axes of crossed polarizers and a low first order interference color elsewhere. Upon inserting a λ plate with its slow axis perpendicular to the line of insertion, as seen in Fig. 3(b), the drops seen in frame (a) show an increased (decreased) color [blue (pale yellow)] along the diagonal perpendicular (parallel) to the slow axis of the plate. This indicates a concentric tangential disposition of the optical axes. In addition, smaller droplets of very low birefringence not seen in frame (a) are also revealed in frame (b). Interestingly, they show an increase in interference color along the diagonal opposite to that of more birefringent drops. Thus, the trace of the optical axes of smaller drops in the layer plane is predominantly radial.

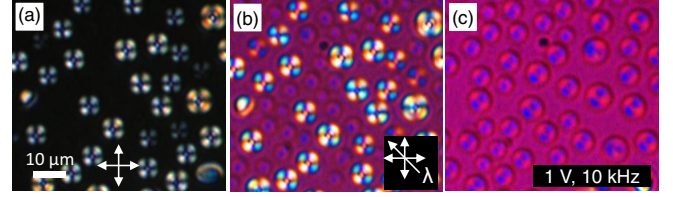


FIG. 3. Typical textures of nematic drops close to the onset of N - I transition in COP5. (a) Concentric drops with extinction crosses and mostly first order white birefringence color. (b) Full wave plate inserted diagonally along northwest direction revealing tiny drops (possibly, bipolar) of very low birefringence hidden in frame (a). (c) Electric Fréedericksz transition from concentric to bipolar structure. Double arrows are crossed polarizers, similarly oriented in all frames. λ plate is inserted in frames (b), (c).

This could correspond to a radial hedgehog or a bipolar drop with its axis along z . If the surface anchoring is tangential as in larger drops, the radial hedgehog geometry cannot normally be expected. However, it has been shown that even with the preferred planar anchoring, nanometric droplets ($R \ll R_c$) could adopt radial geometries, with $\nabla \cdot \mathbf{n} \neq 0$; this is rendered possible by an overriding negative contribution from the saddle-splay constant K_{24} to the free energy of radial droplets [21]. The smaller drops in Fig. 3(b), being of diameter $\approx 5 \mu\text{m}$, appear too large to be affected by K_{24} . We may thus consider them as bipolar, and becoming unstable against the concentric structure under increasing R . This instability gets reversed in an electric field: All the mixtures studied are dielectrically positive, having a Fréedericksz threshold close to 1 V and, upon application of a small electric field, as illustrated in Fig. 3(c), dielectric reorientation ensues so as to transform the escaped concentric drops back to bipolar, with their axes along z .

On suddenly reducing the temperature to well below the N onset, numerous droplets nucleate. Through their growth and coalescence, larger drops with varying morphologies evolve. In Fig. 4, we show several escaped concentric (EC_{XY} and EC_Z) drops, as well as a large bipolar (B_{XY}) drop, derived in this manner (see also Video V1 available in the Supplemental

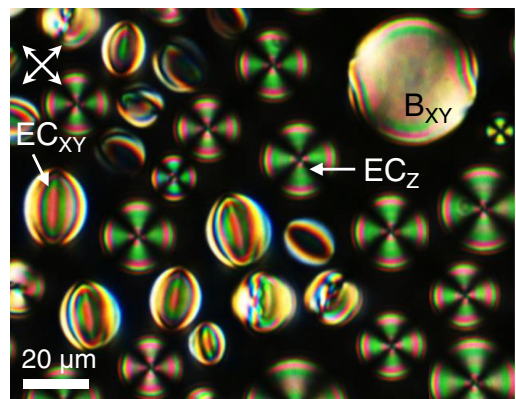


FIG. 4. Bipolar and concentric morphologies evolved through coalescence of smaller droplets in a $20 \mu\text{m}$ thick layer of COP5, planar cell. Diagonally crossed polarizers.

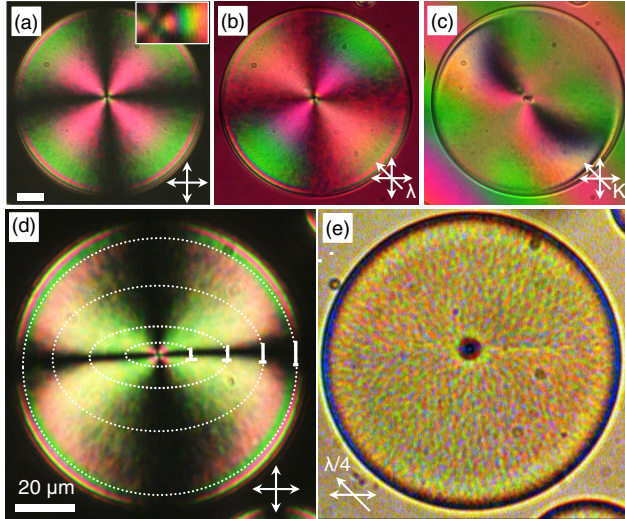


FIG. 5. An escaped concentric drop of the EC_Z type between (a) crossed polarizers P(0)–A(90), (b) P(0)–A(90) with a λ plate, (c) P(0)–A(90) with a K-tilt compensator set for zero path difference in the central region, and along the slow axis in the arrow direction. Inset in (a): Enlarged central region between diagonally crossed polarizers showing the sequence of increasing birefringence colors for increasing radial distance, along x . (d) An escaped concentric drop with elliptical \mathbf{c} director (or \mathbf{n} director trace in the xy plane) lines in a planar cell with the rubbing axis along x . Nails indicate the out-of-layer tilt of the molecules. (e) The SQAM pattern of radiating streaks outlining the director normal \mathbf{n}_\perp . $T = 90^\circ\text{C}$ (a)–(c), 91.4°C (d), (e).

Material (SM) [19]). The least stable of these structures is EC_{XY} and the most stable is EC_Z . The metastable bipolar type B_{XY} is long lived, transforming infrequently into EC_Z (see later).

B. Escaped concentric drops

Now we turn to an elucidation of each of the structurally different drops, starting with the most stable variety, EC_Z . Our identification of these drops as EC_Z is based on the following optical observations. (a) First, the molecular organization in these drops is essentially tangential. With a full wave plate, as shown in Fig. 5(b), we see the birefringence colors becoming more vivid (or shifting to lower order) along the diagonal parallel to the slow axis, compared to the colors along the opposite diagonal. While this indicates a tangential disposition of the optical axis, a more definitive confirmation requires the use of a tilting compensator due to the involvement of higher order interference. On using a Leica K compensator with its slow direction along the axis of rotation [Fig. 5(c)], compensation is obtained along the slow axis for an angle of rotation corresponding to an optical path of approximately $2.4\ \mu\text{m}$. (b) Second, the concentric configuration involves escape into the third dimension as evident from the inset to Fig. 5(a), where the sequence of colors with increasing radius along x goes from first order yellow to second order orange. Thus, if we take the drop as a flattened sphere, as the schematic in Fig. 6(b) indicates, \mathbf{n} is twisted along and about any chosen diameter in the plane $z = \text{constant}$, so that it is

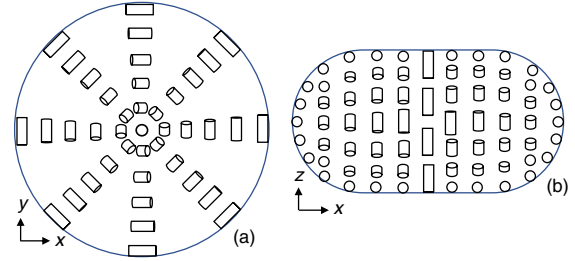


FIG. 6. Idealized director field for the escaped concentric drop EC_Z (imagined as a flattened sphere) in the (a) horizontal ($z = 0$) and (b) vertical ($y = 0$) midplanes. Molecules are shown as cylinders.

parallel to the symmetry axis of the drop in the immediate vicinity of the isotropic core region, and normal to this axis at the interface. With the escaped core, the symmetry axis terminates in two $s = +1$ surface point disclinations, with circular bend lines around them. (c) Lastly, the SQAM pattern that is briefly described in Sec. II provides additional support for considering the drop as of concentric variety. In Fig. 5(e) exemplifying this texture, the stripe images that outline the director normal distribution are noticeably radial. Further, these \mathbf{n}_\perp stripes indicate \mathbf{n} lines to be elliptical rather than circular, corresponding to the texture in Fig. 5(d) in which the extinction brush along x is much narrower than that along y . This asymmetry develops in many EC_Z drops over varied times. This may be seen as an aligning effect in planar cells since elliptical \mathbf{n} lines lead to an overall increase of the director component along x , the rubbing axis.

Notwithstanding the above arguments in favor of viewing the drops in Fig. 5 as EC_Z , we may note that it is hard to distinguish EC_Z from TB_Z definitively by optical microscopy. In several commercial nematic mixtures with K_{33}/K_{11} in the range 0.73–0.94, similar drops have been considered as most probably concentric [4, 13]. For pure CB7CB, 1°C below the N - I point, $K_{33}/K_{11} \approx 0.3$ and $K_{22}/K_{11} \approx 0.4$ [22]. While the K_{33}/K_{11} value here favors the concentric structure, the condition for the TB formation [10, 12], namely, $(K_{22} + 0.431K_{33})/K_{11} \leq 1$, is also satisfied. Assuming the elastic moduli as similarly related in the surfactant doped CB7CB samples studied here, our identification of the EC_Z (as also EC_{XY} ; see later) configuration may be treated as tentative and requiring further investigations to be certain. Simulation of optical textures that takes into account the precise values of all the involved parameters (birefringence, elastic constants, anchoring conditions, polarization state of light, and experimental geometry) is required for a proper differentiation between close structures such as EC_Z and TB_Z (or EC_{XY} and TB_{XY} ; see below).

Next, we consider the escaped concentric variety of drops, EC_{XY} , with their axes in the layer plane. The idealized director field for this case is essentially the same as that shown in Fig. 6, except that, for a drop with its axis along y , the reference axes y and z , as also the horizontal and vertical midsections, now get interchanged. Between crossed polarizers with any azimuth, therefore, light is blocked in the peripheral regions of the four quadrants defined by (x, y) , the drop appearing elliptical in planform, unlike a bipolar drop

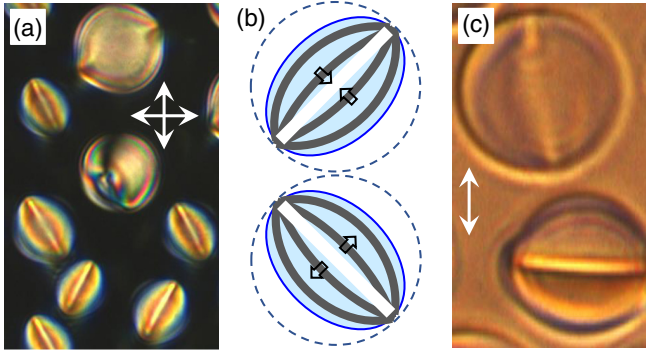


FIG. 7. (a) Drops of EC_{XY} structure appearing elliptical. (b) Schematic of the movement of interference bands (indicated by block arrows) on progressive insertion of a quartz wedge (see Video V2, SM [19]). (c) The dependence of lens action in a drop on the vibration direction of incident linearly polarized light relative to its axis, showing the presence of escaped disclination.

[Fig. 7(a)]. The order of interference fringes decreases with increasing distance from the axis whether or not the defect is singular in core; this causes the fringes to shift as indicated in Fig. 7(b) on a gradual insertion of a quartz wedge (see Video V2, SM [19]). In an earlier study [14], the texture of C_{XY} drops is reproduced in simulation, assuming the absence of escape. The drops observed by us are escaped structures as evident from their polarity-dependent flexoelectro-optic response (see later). Another indication of escape comes from the light-polarization-dependent lens action of the drops (considering the sample thickness as constant in their central region). The characteristic bright line image appearing along the symmetry axis [Fig. 7(a)] is due to the drop acting as a convex cylindrical lens for the extraordinary light vibrating along the axis. Thus, for a drop without escape and with its axis along x , linearly polarized light vibrating along x produces the line image. If, on the other hand, the structure has the escape, the incident beam vibrating along y will only be focused. This is due to the Mauguin wave guiding action [23] that changes the vibration direction from y to x in the sample midplane, provided the optical axis has a π twist along the beam and $(\Delta n)p \gg \lambda$. Here Δn , $p = d$, and λ are the birefringence, pitch of the helical structure, and wavelength of light, respectively. We find that, corresponding to the structure EC_{XY} , the focal line appears strongly in the central region of drops for the incident beam polarized transverse to their symmetry axis, whereas it gets blurred for the beam polarized parallel to it [Fig. 7(c)].

The drops EC_{XY} become unstable once their diameter is greater than the cell thickness and undergo transition to the EC_Z configuration. This is demonstrated in Video V3 (available in the SM [19]), wherein a very slow, continued rotation of the drops EC_{XY} is also discernible. This rotation is quite significant as it occurs in the absence of any electric field. Preliminary results indicate it to be involving vertical thermal gradients (the Lehmann thermomechanical rotation); now efforts are being made for a detailed quantitative examination of the phenomenon under precisely controlled temperature fields (i.e., with a chosen vertical temperature gradient in the

absence of a significant horizontal gradient). The outcome is planned to be reported in due course.

C. Bipolar drops

Coming to bipolar drops B_{XY} , they are readily identified with their characteristic boojums. Large drops of this type formed by coalescing droplets often appear with their axes joining the opposite poles oriented arbitrarily. However, their equilibrium disposition in planar cells requires the axes to be along the rubbing direction. In this orientation, the drops are untwisted, as in Fig. 8(a), in which the extinction of light extends over all of the central region of drops 1–3.

Had the drops been of twisted bipolar structure, due to the Mauguin wave guiding effect, the incident light vibration would, in general, have turned through the twist angle causing light transmission [24]. The SQAM pattern in Fig. 8(b) demonstrates the absence of twist directly and unambiguously. That the optical axis in the central region of bipolar drops is mainly along the bipolar axis is also clear from the optical path compensation seen in Fig. 8(d).

When a bipolar B_{XY} drop is not aligned along the easy axis x , it acquires a structural twist that enhances the free energy. Through a progressive untwisting of the structure with passage of time, its bipolar axis continuously rotates until reaching the equilibrium orientation. This rotation occurs clockwise or counterclockwise depending on whichever sense provides for a faster decay of the twist (see Video V4 in the SM [19]). For example, in Fig. 9, while frames (a–c) of a time series show clockwise rotation, frames (d–f) of another series show counterclockwise rotation. That the rotation is not a rigid body motion but an apparent effect of structural untwisting is obvious from the continued extinction of light observed, under crossed polarizers $P(0)$ – $A(90)$, all over the drops, except in a narrow boundary region (see Video V5 in the SM [19]). The molecular alignment on the flat top and bottom faces of the drops remains planar throughout (along x) even as the twist across the thickness relaxes. The incident light vibrating along x follows the twist [23] to emerge vibrating again along x and be blocked by the analyzer.

We present in Fig. 10 the data on time variation of angular deviation $\alpha(t)$ of the bipolar axis for three different size drops. It is evident from the exponential variation of $\alpha(t)$ that the angular velocity $d\alpha/dt$ varies as α , leading to $\alpha = \alpha_0 e^{-t/\tau}$ with τ as the relaxation time and α_0 as the maximum tilt of the bipolar axis at $t = 0$. The situation here is very similar to that of the sample relaxing in zero field from the twist Fréedericksz state. Analogously, we may expect τ to be determined by the effective rotational viscosity γ , elastic constant K_{22} , and sample thickness d . Relaxation time for the usual twist Fréedericksz state is given by $\tau\pi^2 K_{22} = \gamma d^2$ [25]. For an order of magnitude estimate of effective γ here, we may take $\langle \tau \rangle \approx 200$ s corresponding to the plots (b,c) in Fig. 10; with $K_{22} = 1$ pN and $d = 20$ μm , we get $\gamma \approx 6$ Pa s, which is greater by an order compared to the known value of γ (≈ 0.3 Pa s) in a twist-bend nematogenic mixture near the N onset point [26]. This is not surprising considering that the drop subjected to boundary conditions all over its surface is a 3D system, unlike an extended planar nematic slab with a twist distortion varying in one direction.

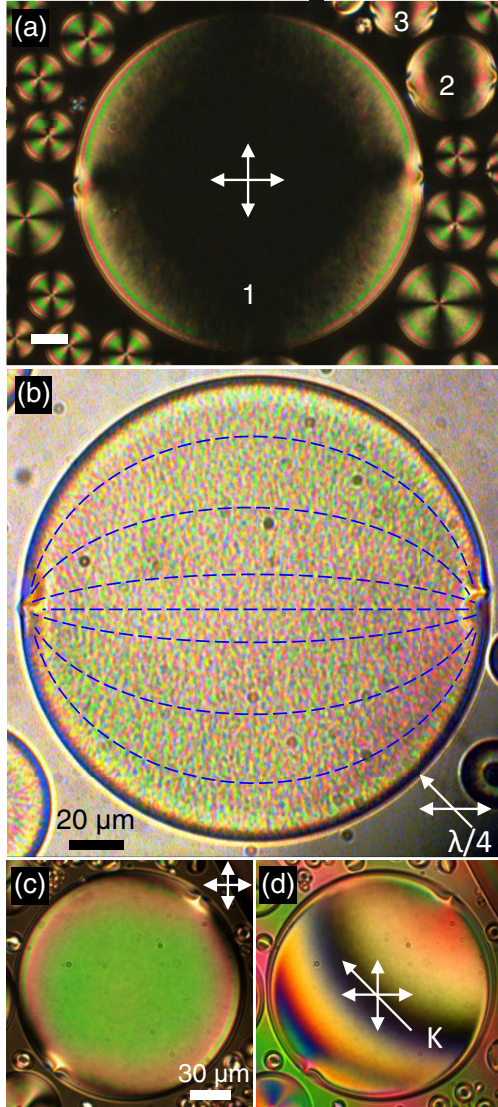


FIG. 8. Untwisted bipolar drops B_{XY} with their axes along the rubbing direction, corresponding to the equilibrium configuration. (a) Extinction of light all over the inner region of bipolar drops 1–3 for P(0)–A(90) indicating the absence of twist in drops of varied sizes. (b) SQAM pattern showing the stripes along the director normal corresponding to the director profile indicated by dashed (blue) lines. (c) A B_{XY} drop diagonally oriented relative to crossed polarizers, showing higher order interference colors. (d) The drop in (c) with a tilt compensator K in the position of zero path along its slow axis, showing the \mathbf{n} alignment along the bipolar axis. Double arrows indicate axes of polarizers. $T = 91.9^\circ\text{C}$ (a), 91.4°C (b)–(d).

Bipolar drops B_{XY} oriented in their equilibrium position along x are stable in all sizes. However, the drops oblique to x and in the dynamical process of structural untwisting switch to the EC_Z configuration occasionally. This aspect is illustrated by the select time frames in Fig. 11 (see Video V6 in the SM [19]). The clockwise rotation of the bipolar axis in (a) stops when the transformation to EC_Z begins with the poles shifting toward each other (b,c) and the new equilibrium geometry (d) is established after a few minutes.

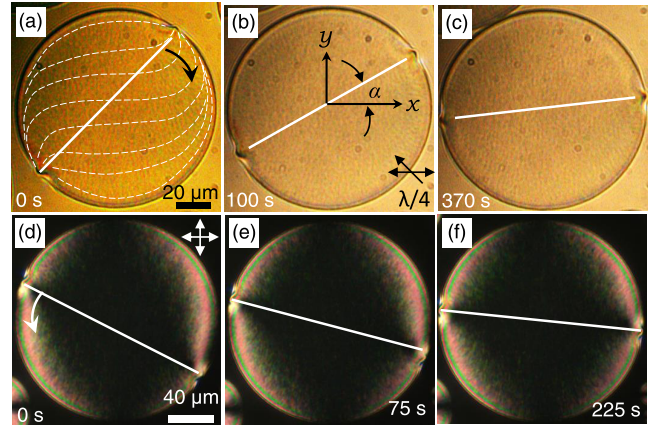


FIG. 9. Select frames from two time-image series showing clockwise (a)–(c) and counterclockwise (d)–(f) rotations of the bipolar axis. The dashed lines in (a) indicate the surface director field from the SQAM pattern; the director is oriented along the easy axis in the central region of the flattened faces of the drops. The angle $\alpha(t)$ made by the bipolar axis with x at any given time determines the degree of twist across the sample. Light extinction over the inner region of drops under crossed polarizers, P(0)–A(90), is due to the Mauguin wave guiding effect [23]. This extinction is maintained all through the rotation process [see frames (d)–(f)]. $T = 91.5^\circ\text{C}$.

D. Drops with a pair of $+\frac{1}{2}$ lines or a $+\frac{1}{2}$ line-boojum combination

In a mixture with a sufficiently high surfactant concentration as, for example, in COP5, the N phase in the form of dispersed droplets coexists with the isotropic down to the temperature of its transition to the N_{TB} phase. After the transformation of the N phase is complete, the resulting N_{TB} phase also forms drops dispersed in the extended isotropic phase. Upon heating the sample from this biphasic state back to the N - I state, the N droplets that form are mostly found with an uncommon configuration. As exemplified in Fig. 12(a), in planar cells held between crossed polarizers P(0)–A(90), the corresponding texture contains a pair of “two-brush” defects

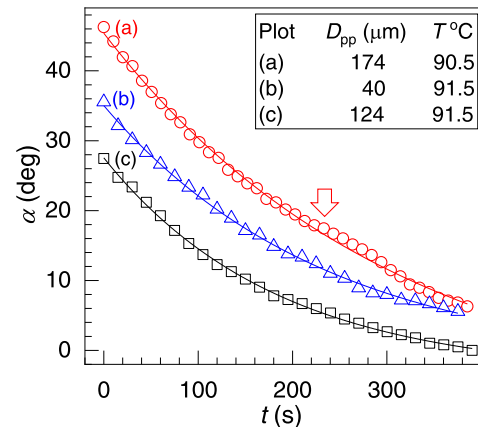


FIG. 10. Rotation of the bipolar axis toward the rubbing axis in a planar cell. D_{pp} denotes the pole-to-pole diameter of the drops. Continuous lines are exponential fits. The arrow in (a) points to the retarding effect of a neighboring drop (see Video V4 in the SM [19]).

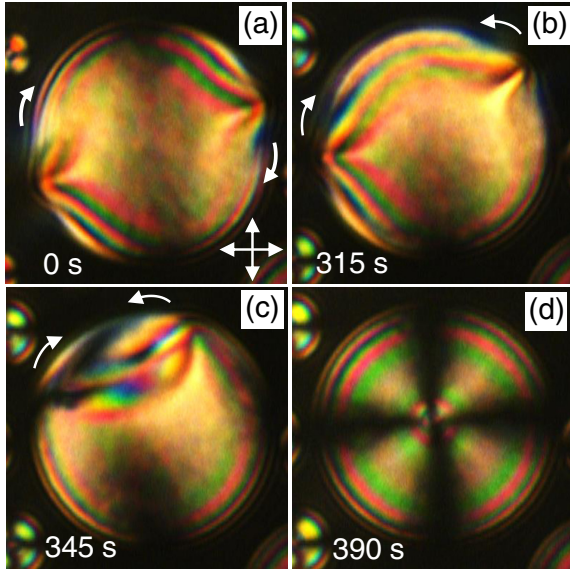


FIG. 11. Twisted bipolar drop TB_{XY} rotating clockwise toward the equilibrium position (a) stops abruptly and then transforms into the EC_Z configuration (b)–(d). $T = 92^\circ C$.

located away from the boundary and symmetrically on either side of the center. The two $+\frac{1}{2}$ singular disclinations that they represent appear as dark spots in natural light or when using a single polarizer. In Fig. 12(b) depicting the SQAM pattern,

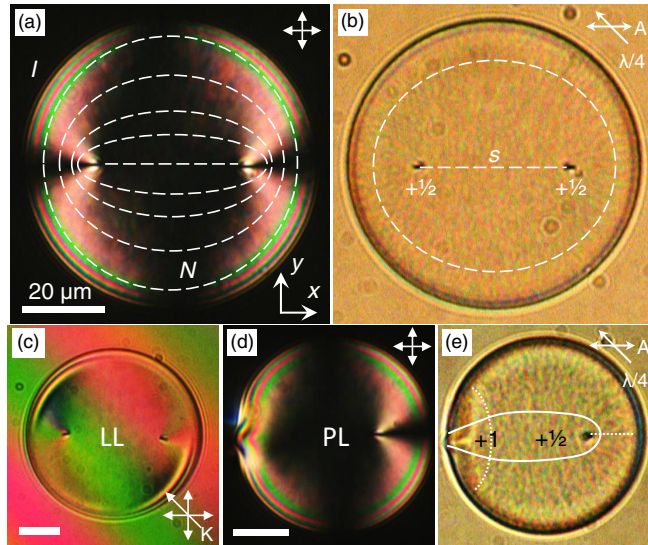


FIG. 12. (a) A drop of the type LL with a pair of disclination lines of strength $+\frac{1}{2}$ at the nodes from where two extinction brushes emerge. (b) The SQAM pattern of the drop LL showing short streaks along the director normal; white dashes in (a), (b) indicate the \mathbf{n} distribution. (c) Texture of the LL drop on using a tilt K compensator set to obtain extinction in diagonally opposite peripheral regions where \mathbf{n} is perpendicular to the slow axis of the compensator, the corresponding path difference being approximately $2.7 \mu m$. (d) A drop denoted by PL with a boojum and a single $+\frac{1}{2}$ line defect. (e) The SQAM texture of the PL drop wherein the short stripes outline \mathbf{n}_\perp ; the dotted and continuous white lines are the \mathbf{n} and \mathbf{n}_\perp flux lines, respectively. $T = 91^\circ C$ (a), (b), $91.5^\circ C$ (c), $91.1^\circ C$ (d), (e).

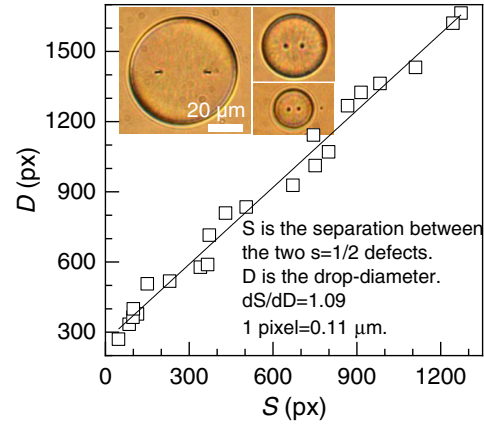


FIG. 13. Linear variation of the distance S of separation between two $+\frac{1}{2}$ lines with diameter D of the drop. Inset shows select drops from a time series recorded as the size decreased due to an increase in T .

the \mathbf{n}_\perp field around these spots is outlined by the short stripes, while the dashed white lines indicate the \mathbf{n} field. The indicated director field is also in conformity with the extinction regions seen in Fig. 12(c) using crossed polarizers with a tilting K compensator.

The separation S between the half lines in an LL drop is a linear function of the drop diameter D . Figure 13, which is from measurements on drops of different diameters found at a given temperature, illustrates this variation (see also Video V7 available in the SM [19] showing a drop decreasing continuously in size following a small increment in temperature). For a large drop, the lines situated in the curved boundary region appear to drift to opposite poles to shorten their length or, equivalently, the distortion energy, and thereby turn into boojums. In the other extreme, in very small drops, the lines combine to yield a concentric drop with a $+1$ vertical line through the center. As mentioned in the Introduction, for disklike 2D nematic systems, the possible defect structures have been analyzed earlier for their stability under various boundary conditions [15]. With the director \mathbf{n} lying tangentially in the xy plane at the interface, and for low values of temperature and elastic parameters, the LL configuration is predicted by the Landau–de Gennes approach to be the stablest. A nonsingular harmonic map solution corresponding to the escaped concentric $+1$ structure is also found admissible when the temperature is low and elastic constant is very small. Clearly, these conjectures are in broad agreement with our observation of LL and EC_Z configurations. We may note that the LL configuration has been lately of considerable interest in the area of active nematics in which self-propelling half-integer defects frequently form pairs; one of them is the “bound vortex” LL pair representing, in effect, the $+1$ circular geometry; the other two are the “bound aster” and “bound spiral” defects, which equivalently are the radial and spiral $+1$ defects [27,28].

E. Drops with multiple defects

In the early stages of the formation of a large N drop through aggregation of numerous finely divided N droplets,

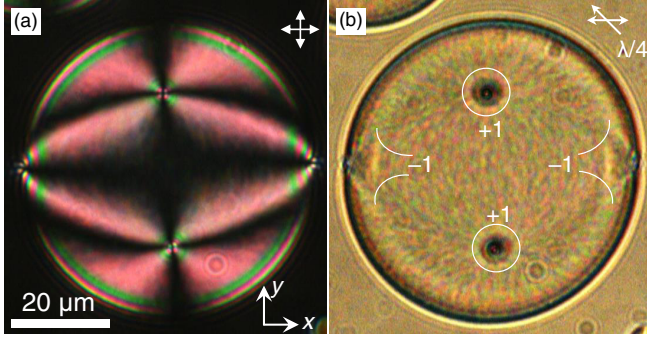


FIG. 14. A nematic drop in its metastable configuration involving two boojums, each with a surface charge of -1 , and two interior $+1$ disclinations, each with a surface charge of $+2$. The short stripes in the SQAM pattern (b) indicate the orientation of \mathbf{n}_\perp . The $+1$ defects are circular and the boojums are hyperbolic (indicated by white lines). $T = 90^\circ\text{C}$.

varied nonequilibrium defect configurations emerge. While the number and nature of defects may be arbitrary, the Poincaré-Hopf restriction on the total topological charge applies all through the course of equilibration that involves annihilation of opposite defects. Depending on the symmetry of organization of defects, some higher energy structures with a greater number of defects than corresponding to an energy minimum may come to exist in an unstable or metastable state. A relatively stable multiple defect structure that is frequently found is shown in Fig. 14. If the symmetry of this structure is perturbed due to thermal fluctuations or neighboring drops, the boojums slide on the boundary toward one of the line disclinations that is closer to them and all three defects are eventually annihilated. Large N drops with multiple defects are like 2D objects; they are N islands mostly planarly aligned in the central part and surrounded by the isotropic. The boojums form on the meniscus separating the nematic and isotropic phases, while linear disclinations occur within the flat region just as in any planar sandwich cell.

F. Size-dependent configurations of drops

From the foregoing description of various possible director fields within the drops, it is evident that at a given temperature (on which the elastic and anchoring parameters depend)

and concentration of the surfactant (on which the transition temperatures and the biphasic range depend), it is the drop size that plays a key role in determining the equilibrium structure(s). As previously noted, the effect of drop size on the stability of different director patterns in nematic drops with tangential boundary conditions and very low bend elastic modulus has been theoretically studied [16]. The drops considered therein, being free of any external aligning influence, may be compared with the drops with $D \leq d$ observed here. We show in Table I the structures corresponding to different droplet diameters predicted in [16] and observed here. Except for LL and PL configurations, the others can all be realized at any temperature below the onset point of the N phase. This is because, on reducing T marginally, new drops nucleate randomly and grow along with previously existing ones, so that drops of varying size come to exist. Drops of the type LL and PL form at the $N_{\text{TB}}-N$ transition.

G. Fréedericksz distortion in N drops

In the high frequency regime in which ionic effects become negligible, the drops are destabilized only by the dielectric torque. The sequence of orientational changes that occur in a B_{XY} drop, as the voltage is gradually increased, is presented in Figs. 15(a)–15(i). The drops B_{XY} , EC_Z , and LL are all very similar in their voltage determined structural features (see Figs. S1 and S2 in the SM [19]), particularly in the final stages of reorientation corresponding to Figs. 15(j)–15(l). The transition in all cases shows a nonzero threshold, below 1 V, at which a change in the birefringence color pattern is clearly discerned. For example, in COP5, the threshold is 0.8 V. This contrasts with an earlier observation of electric distortion taking place without a critical field in bipolar drops [29]. In COP5, as in other cases previously examined [29,30], the initial realignment occurs at the interface; between crossed polarizers, with the homeotropic boundary regions extinct, the birefringent drop assumes an oval-like aspect [Figs. 15(b) and 15(c)]. Further, the original boojums appear shifted out of the xy midplane in opposite directions so that they are seen as four-brush surface defects close to the boundary [Figs. 15(b)–15(f)]. This implies an out-of-plane tilt of the bipolar axis, as in Ref. [29]. As the distortion extends inward at higher voltages, a narrow bright band develops between the north and south poles. This is likely to be due to a Brochard-Leger-type

TABLE I. Configuration of drops for various diameters.

D (μm)	Configurations		Remarks
	Observed ^a	In Ref. [16] ^b	
4	B	$B(D \leq 9.6 \mu\text{m})$	See Fig. 4.
8	EC_{XY}, EC_Z	B	See Fig. 4. EC_{XY} and TB_{XY} are hard to tell apart by optical textures.
12	EC_{XY}, EC_Z	B or EC bistable	See Fig. 5.
16	EC_{XY}, EC_Z	EC	See Fig. 5.
≥ 20	B_{XY}, EC_Z, LL, PL	EC	See Fig. 13. B_{XY} aligned along the rubbing axis R is stable; when its axis is inclined to R , it occurs as TB_{XY} which is metastable. LL and PL occur only on heating the N_{TB} phase to the N .

^aIn a 20 μm thick layer of COP5 in a planar cell.

^bFor $K_{11} = 9.5 \text{ pN}$, $K_{22} = 8 \text{ pN}$, $K_{33} = 6 \text{ pN}$, $W = 100 \mu\text{J}/\text{m}^2$ and $D \leq 32 \mu\text{m}$.

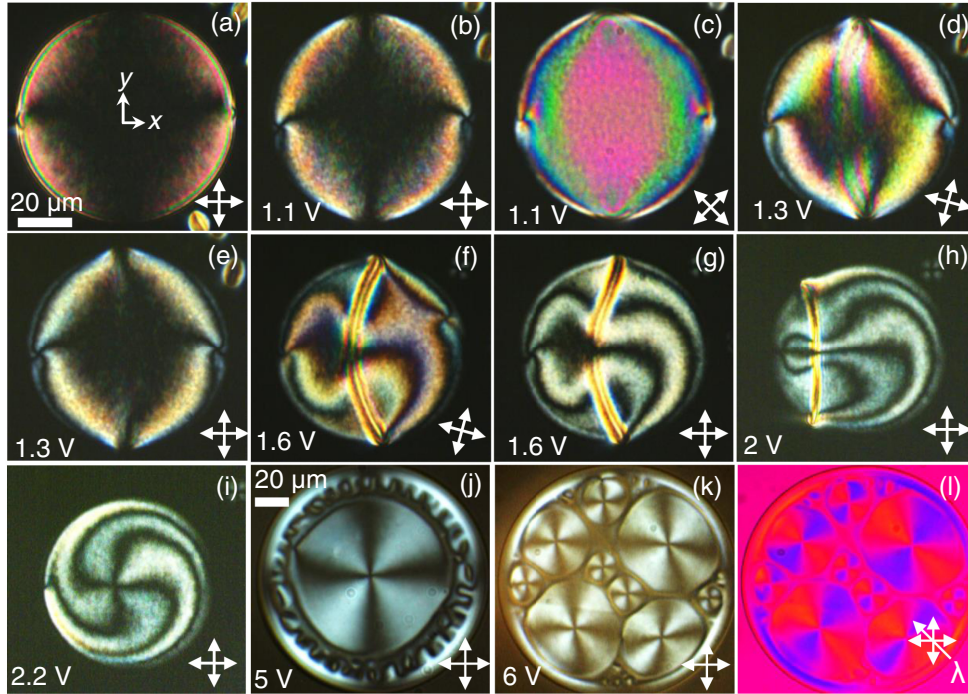


FIG. 15. The course of Fréedericksz reorientation in nematic drops with increasing voltage of a sine wave field of frequency 10 kHz. (a)–(i) COP5 at 95 °C. (j)–(l) Final stage of reorientation of a LL drop at 92 °C showing division of the drop into many smaller bipolar drops, each with a surface charge 2.

[31,32] wall building up in the yz meridional plane. While, in the midplane xz , it involves only the splay-bend strain, the twist enters into it increasingly for other xz planes, as we move away from the $y = 0$ plane. In fact, it is possible to visualize two such walls against each other, located on either side of the midplane $z = 0$. The lensing property of these walls offers an explanation for the appearance of the band such as in Fig. 15(d). It is also likely that the wall evolves into a $+1$ disclination of the concentric structure in the next stage of growing distortion. This line progressively drifts to a side and disappears eventually [Figs. 15(f)–15(h)], a behavior also seen with the $+1$ line in EC_{XY} drops switching to EC_Z under an electric field. In the penultimate stage of the Fréedericksz state, as seen in Fig. 15(i), the bright band between the north-south poles and the boojums disappear, leaving a centered spiral extinction cross. It is notable that the drop does not turn completely homeotropic and defect free, even at high voltages; we tested this up to 30 V. In its quasihomeotropic defect state, the birefringence becomes so low that very long exposures become necessary to photograph the texture. The structure to which the spiral texture belongs is a matter of conjecture, since, deep in the Fréedericksz state, it is hard to optically distinguish between the twisted bipolar and escaped $+1$ configurations, both with their axes along the observation direction. We will, therefore, refer to the structure simply as the spiral defect. The final stage of distortion is marked by a complex instability developing in the peripheral region, as in Fig. 15(j). It culminates in the formation of many tiny droplets each with an extinction cross between crossed polarizers [Fig. 15(k)]. The structure of these drops, from the color changes that occur on inserting a λ plate [Fig. 15(l)], involves a significant radial component of the director field

as in a bipolar configuration. It is interesting that the original large drop, under a large field, instead of assuming a homeotropic geometry, prefers to divide itself into a multitude of droplets each with a surface charge of 2, as stipulated by the Poincaré-Hopf theorem.

H. Flexoelectro-optic effect in escaped concentric drops

First, we consider the response of escaped concentric drops EC_Z to an applied square-wave field of low frequency. Whereas the distortion in a high frequency (above ~ 10 kHz) field is exclusively of dielectric origin, that in the regime of static or quasistatic fields is subjected additionally to competing flexoelectric and electroconvective effects. The electrical conductivity of the mixtures is large, of the order of $\mu\text{S}/\text{m}$ [18]. Thus, when U is also low, the flexoelectric contribution to free energy becomes predominant, since the electrical double layers significantly reduce the bulk field so as to render the dielectric response minimal or negligible [33]. Experimentally, this becomes evident from the flexoelectro-optic (FEO) effect found in escaped concentric structures, whether EC_{XY} or EC_Z . This effect, discovered by Patel and Meyer in cholesterics [34], refers to the rotation of the local director, or equivalently the macroscopic optic axis, about the direction of the electric field \mathbf{E} acting transversely to the helix axis; it causes a periodic splay-bend strain of the \mathbf{n} field, generating thereby a net inverse flexoelectric polarization along \mathbf{E} . The angle β by which the helix axis turns is shown to be given $\tan \beta = eE/(qK)$, where K is the average of K_{11} and K_{33} , e is the average of the splay and bend flexoelectric coefficients e_s and e_b , and q is the helical wave vector [34]. For a given field \mathbf{E} , therefore, rotational sense depends on the sign of \mathbf{q} .

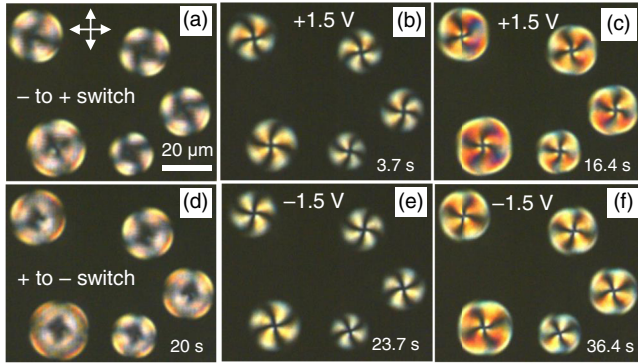


FIG. 16. Select frames from a time series showing flexoelectro-optic effect in EC_z drops of CTA5 at 92°C . SQW excitation; $f = 0.025$ Hz. Polarity switches from $-$ to $+$ at $t = 0$ in (a); birefringence of drops increases from (b) to (c) following the polarity change. It reflects a decrease in the bulk voltage under ion transport and buildup of surface field. (e), (f) are similar to (b), (c) except for a reversal of the spiral sense across the polarity switch.

In a twisted nematic composed of achiral molecules in which right and left twists are energetically degenerate, clockwise and anticlockwise rotations corresponding to opposite signs of \mathbf{q} are equally probable. Referring now to Fig. 6 for EC_z , when a low frequency square wave (SQW) field acts along z , the helical axes of the twisted structure confined to the xy plane rotate about the layer normal through β due to the FEO effect. Optically, between crossed polarizers, this is revealed by a rotation of extinction brushes by the same angle. In Fig. 16 demonstrating the effect (see Video V8 in the SM [19]), the drops are expectedly found to exhibit spiral extinction brushes of either handedness. With the FEO rotation of the local director by a constant angle, the concentric circles of the c -director field around an escaped $+1$ defect change into logarithmic spirals; this gets reflected in the spiral extinction brushes of handedness opposite to that of the c lines. It is relevant to note that the FEO effect has previously been observed for both twisted bipolar drops [35] and $s = \pm 1$ line disclinations in alignment inversion walls [36]; for the latter case, theoretical analyses are also reported [37,38].

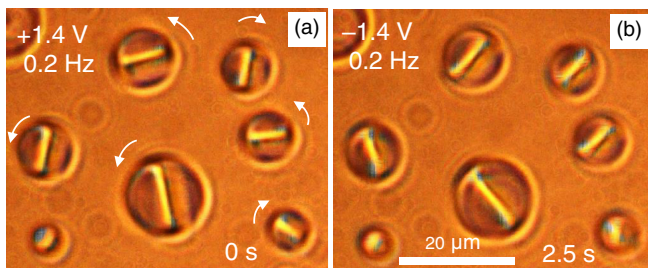


FIG. 17. Escaped concentric drops EC_{XY} of CTA5 at 92°C under excitation by a SQW field of frequency $f = 0.2$ Hz and voltage $U = 1.4$ V. Frames (a), (b) are from a time series, captured after successive polarity reversals showing maximum deviations for opposite fields. Arrows in (a) indicate the sense in which the flexoelectro-optic rotation would take place at the next polarity switch.

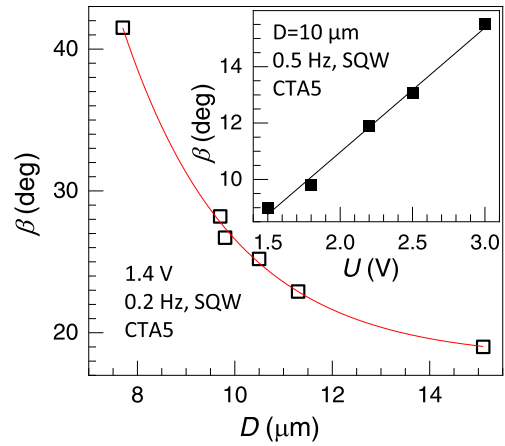


FIG. 18. Angle of rotation β as a function diameter D of the escaped concentric drop EC_{XY} ; CTA5 at 92°C , subjected to 1.4 V SQW; 2β is the angle between extreme positions of the axis of the drop corresponding to the two opposite field directions. Inset: Linear variation of β with voltage U of a SQW field.

The FEO effect in drops EC_{XY} finds essentially the same explanation as the one provided above for drops EC_z . The director field for an EC_{XY} drop in the midplane xy , in the field-free state, may be represented as in Fig. 6(b), except that the cross section now is circular, instead of being oval-like. Thus, with the twist axis x rotating in the layer plane due to the FEO effect, the axis of symmetry also shifts concomitantly in the same plane. We may note that EC_{XY} drops are mostly spherical ($D < d$) and free from the aligning influence of the substrates. If we imagine such a drop as a stack of thin layers along z , the effective pitch decreases progressively away from the middle layer. This complicates the FEO rotation and what we obtain is some average effect. The observed rotation in CTA5 excited by a SQW field of frequency 0.2 Hz is illustrated in Fig. 17 (see Video V9 in the SM [19]). The extent of rotation is found to decrease exponentially with increasing diameter of the drops (Fig. 18). It decreases also with increasing frequency, becoming practically undetectable above 5 Hz. As expected of a flexoelectric phenomenon, and as the inset to Fig. 18 shows, the rotation angle is linear in the applied electric field.

IV. CONCLUSIONS

In this study, we have demonstrated the morphological richness of nematic drops dispersed in the isotropic phase, in binary mixtures of the twist-bend mesogen CB7CB with a surfactant, such as 2-octadecoxypropanol. The combination of extremely low bend elastic constant that characterizes the nematic phase of twist-bend nematogens and the extended $N-I$ biphasic region due to the addition of a surfactant make these systems ideal media to realize some less common geometries of the director field. This is exemplified by the escaped concentric, bound vortex, and boojum-line configurations obtained here under tangential boundary conditions. The bipolar configuration, which is more common in calamitics with a large bend modulus, is also seen in our samples; in flattened spherical drops subjected to planar substrate conditions, it

occurs with its axis along the easy axis (B_{XY}), being a less stable variant than the most stable escaped concentric structure EC_Z with its symmetry axis along the layer normal; it switches occasionally to the EC_Z modification when transiting from its twisted TB_{XY} to the untwisted equilibrium state, B_{XY} . The EC_{XY} configuration obtained only in the small-size regime ($D < d$) transforms into EC_Z as it enters the large size regime ($D > d$). Notably, in the absence of an external electric field, the EC_{XY} drops rotate continuously about the layer normal and this thermomechanical-like effect is currently being closely examined for its precise characterization, and we expect to report the results in the near future. As a bridge between the B_{XY} and EC_Z structures, there occurs the bound vortex configuration LL with a pair of $+\frac{1}{2}$ line disclinations predicted recently. A hybrid variety PL, with a single pole (boojum) and a single $+\frac{1}{2}$ line, is also found as a stable

structure. In low frequency fields, the escaped character of the concentric drops reveals itself through their flexoelectro-optic response. Remarkably, in high frequency, high voltage electric fields, all the structurally differing drops (EC_Z , B_{XY} , LL, and PL), instead of reorienting homeotropically, divide into many smaller drops, each of them with a surface charge 2, as prescribed by topology.

ACKNOWLEDGMENTS

The authors are grateful to Professor B. L. V. Prasad for the experimental facilities. C.V.Y. and D.S.S.R. acknowledge the financial support from the Science and Engineering Research Board (SERB), Department of Science and Technology [DST], Government of India, under Projects No. CRG/2020/001779 and No. CRG/2019/001671.

-
- [1] J. L. Ferguson, *SID Int. Symp. Dig. Tech.* **16**, 68 (1985).
 [2] J. W. Doane, N. A. Vaz, B.-G. Wu, and S. Zumer, *Appl. Phys. Lett.* **48**, 269 (1986).
 [3] P. S. Drzaic, *J. Appl. Phys.* **60**, 2142 (1986).
 [4] P. S. Drzaic, *Liquid Crystal Dispersions* (World Scientific, London, 1995).
 [5] G. P. Crawford and S. Zumer, *Liquid Crystals in Complex Geometries* (Taylor & Francis, London, 1996).
 [6] M. Kleman and O. D. Lavrentovich, *Philos. Mag.* **86**, 4117 (2006).
 [7] M. Kleman and O. D. Lavrentovich, *Soft Matter Physics: An Introduction* (Springer, New York, 2003).
 [8] O. O. Prishchepa, A. V. Shabanov, and V. Ya. Zyryanov, *Phys. Rev. E* **72**, 031712 (2005).
 [9] G. E. Volovik and O. D. Lavrentovich, *Sov. Phys. JETP* **58**, 1159 (1983).
 [10] R. D. Kamien, *Rev. Mod. Phys.* **74**, 953 (2002).
 [11] D. Crowley and M. Grant, *J. Geom. Phys.* **117**, 187 (2017).
 [12] R. D. Williams, *J. Phys. A* **19**, 3211 (1986).
 [13] P. Drzaic, *Mol. Cryst. Liq. Cryst.* **154**, 289 (1988).
 [14] J. Jiang and D.-K. Yang, *Liq. Cryst.* **45**, 102 (2018).
 [15] Y. Hu, Y. Qu, and P. Zhang, *Commun. Comput. Phys.* **19**, 354 (2016).
 [16] J. Wu, H. Ma, S. Chen, X. Zhou, and Z. Zhang, *Liq. Cryst.* **47**, 1698 (2020).
 [17] K. S. Krishnamurthy, D. S. Shankar Rao, M. B. Kanakala, C. V. Yelamaggad, and M. Kleman, *Soft Matter* **16**, 7479 (2020).
 [18] K. S. Krishnamurthy, D. S. Shankar Rao, M. B. Kanakala, and C. V. Yelamaggad, *Phys. Rev. E* **103**, 042701 (2021).
 [19] See Supplemental Material at <http://link.aps.org/supplemental/10.1103/PhysRevE.105.024709> for Videos V1.avi–V9.avi and the file SM.pdf containing explanatory notes on the video clips and some optical textures.
 [20] K. S. Krishnamurthy, M. B. Kanakala, C. V. Yelamaggad, and N. V. Madhusudana, *J. Phys. Chem. B* **123**, 1423 (2019).
 [21] V. Tomar, S. I. Hernández, N. L. Abbott, J. P. Hernández-Ortiz, and J. J. de Pablo, *Soft Matter* **8**, 8679 (2012).
 [22] G. Babakhanova, Z. Parsouzi, S. Paladugu, H. Wang, Yu. A. Nastishin, S. V. Shiyonovskii, S. Sprunt, and O. D. Lavrentovich, *Phys. Rev. E* **96**, 062704 (2017).
 [23] C. Mauguin, *Bull. Soc. Fr. Miner.* **34**, 3 (1911).
 [24] O. D. Lavrentovich and V. V. Sergan, *Nuovo Cimento* **12**, 1219 (1990).
 [25] P. Oswald and P. Pieranski, *Nematic and Cholesteric Liquid Crystals* (Taylor & Francis, New York, 2005).
 [26] C. Meyer, P. Davidson, D. Constantin, V. Sergan, D. Stoenescu, A. Knežević, I. Dokli, A. Lesac, and I. Dozov, *Phys. Rev. X* **11**, 031012 (2021).
 [27] K. Thijssen and A. Doostmohammadi, *Phys. Rev. Res.* **2**, 042008 (2020).
 [28] F. Vafa, Geometry and dynamics of active topological defects, Ph. D. thesis, University of California, Santa Barbara, 2021, available online at <https://escholarship.org/uc/item/9v38m6jm>.
 [29] A. Fernández-Nieves, D. R. Link, D. Rudhardt, and D. A. Weitz, *Phys. Rev. Lett.* **92**, 105503 (2004).
 [30] S. Kralj and S. Žumer, *Phys. Rev. A* **45**, 2461 (1992).
 [31] F. Brochard, *J. Phys. (Paris)* **33**, 607 (1972).
 [32] L. Léger, *Mol. Cryst. Liq. Cryst.* **24**, 33 (1973).
 [33] K. S. Krishnamurthy, *Phys. Rev. E* **89**, 052508 (2014).
 [34] J. S. Patel and R. B. Meyer, *Phys. Rev. Lett.* **58**, 1538 (1987).
 [35] P. Rudquist, E. Körblová, D. M. Walba, R. Shao, N. A. Clark, and J. E. MacLennan, *Liq. Cryst.* **26**, 1555 (1999).
 [36] P. Kumar and K. S. Krishnamurthy, *Liq. Cryst.* **33**, 131 (2006).
 [37] Y. Tian and Z. D. Zhang, *Liq. Cryst.* **42**, 288 (2015).
 [38] G.-L. Zheng, H. Zhang, W.-J. Ye, Z.-D. Zhang, H.-W. Song, and L. Xuan, *Chin. Phys. B* **25**, 036101 (2016).